Lowering temperature of Cu sinter bonding under low-pressure in ambient air by in-situ generation and reduction of Cu_2O nanoparticles

Miwa Oba[a], Tomoki Matsuda[a,*], Masashi Dougakiuchi[a,b], Shio Okubo[a], Makoto Kambara[a]

[a] Division of Materials and Manufacturing Science, Graduate School of Engineering, The University of Osaka

[b] Shimane Institute for Industrial Technology, 1 Hokuryo-cho, Matsue, Shimane, 690-0816, Japan

[*]**Corresponding author**: Tomoki Matsuda

Email: t-matsu@mapse.eng.osaka-u.ac.jp

Phone: +81-6-6879-7551, Fax: +81-6-6879-7551

Address: 2-1 Yamadaoka, Suita, 565-0871 Osaka, Japan

Abstract

Cu sinter bonding has emerged as a promising technology for highly reliable electronic packaging due to its low cost and excellent electrical and thermal conductivity. However, Cu particles are prone to oxidation, and their sinterability decreases significantly at lower temperatures, requiring high-pressure or controlled atmospheric conditions at elevated temperatures. This study investigated reducing the bonding temperature of Cu sinter bonding under low bonding pressure in ambient air by utilizing the in-situ oxidation and subsequent reduction of the Cu surface, leading to the formation of Cu nanoparticles. Slightly oxidized Cu particles were prepared through a plasma flash evaporation process under an Ar-H_2 plasma, followed by vacuum refrigeration. These particles were used to facilitate surface reactions with polyethylene glycol (PEG400) during the bonding process. We found that the prepared particles contributed to lowering the reduction temperature through the temporary formation of Cu_2O nanoparticles. These nanoparticles, precipitating above 160 °C from Cu complexed with PEG400, were subsequently reduced to Cu nanoparticles. The generated Cu nanoparticles acted as bridges among Cu fine particles, enhancing sinterability. Consequently, Cu-Cu sinter bonding was achieved at 220 °C under 0.3 MPa in ambient air, forming a sufficiently sintered Cu layer. This approach offers a pathway for low-temperature, low-pressure bonding suitable for industrial-scale applications.

Keywords: Cu sinter bonding; Plasma flash evaporation (PFE); In-situ oxidation and reduction; Cuprous oxide; Polyethylene glycol (PEG400)

1.Introduction

Die bonding materials used in electronic packaging for power modules are required to operate reliably at temperatures above 200 °C [1–4]. While Sn-Pb solders have conventionally been used for high temperature die-bonding, restrictions on the use of Pb have been implemented due to the growing environmental concerns [5–7]. Sinter bonding with metallic fine particles has emerged as a promising alternative to Sn-Pb solders, offering low-temperature bondability and superior heat resistance [8–10]. Among sinter materials, Ag and Cu have been widely studied because of their high electrical and thermal conductivity [11,12]. In particular, Cu particles exhibit advantages such as lower cost and superior thermal durability compared to Ag particles, although their sensitivity to oxidation in air remains a notable challenge [12,13]. Since the oxide layer formed on the Cu surface hinders the sintering, high bonding pressure (≥5 MPa) [14–17] or controlled atmosphere [18–20] are employed to prevent Cu oxidation during the bonding process. Moreover, bonding temperatures typically exceed 250 °C to ensure sufficient bonding strength as the driving force for Cu sintering diminishes at lower temperatures or lower pressure [19,21]. However, bonding under low-pressure in ambient air is highly desirable for mass industrial production, as high-pressure or atmosphere-controlled process increase complexity and the risk of chip damage [12,21]. Furthermore, lower bonding temperature are preferred to minimize structural damage to the substrate [18,22].

To address the challenges associated with bonding conditions, we leverage existing knowledge for bonding under low pressure and ambient atmosphere, while proposing the use of Cu particles with controlled size and oxidation, combined with a reducing organic solvent, as a novel approach to achieve bonding at lower temperatures. In low-pressure bonding, Cu particles with surface oxide have been used as bonding materials, where Cu nanoparticles generated through the reduction of surface oxide contribute directly to sintering [19,23]. During the bonding process, Cu nanoparticles are widely formed on the surface of submicron Cu particles, acting as a driving force to form bridges among the particles. The sintered layer becomes dense through the incorporation of generated nanoparticles into submicron particles. For bonding in ambient air, reducing organic solvents are utilized not only to induce the reduction of Cu oxide but also to provide oxidation resistance during bonding [16,21,24]. These approaches have enabled low-pressure bonding in air; however, achieving bonding at low temperatures (< 250 °C) remains a technical limitation. In the sintering process utilizing the surface oxide of Cu particles, previous studies have reported that the reduction of Cu_2O begins at approximately 220 °C, indicating its applicability for low-temperature bonding. However, complete reduction requires higher temperatures due to the prolonged reduction time, even in oxygen-free atmospheres [19]. This suggests that limiting the amount of oxide could effectively shorten the reduction time and lower the temperature required for complete reduction. Therefore, for low-pressure bonding, we focus on producing nano- to submicron-sized particles with suppressed surface oxidation.

As a method for synthesizing particles, chemical synthesis is widely used as it allows the production of nanoparticles from metal precursors using reducing agents [25–28]. However, the synthesized nanoparticles are typically stabilized with a capping agent to minimize oxidation and control crystal growth [28]. In this respect, a gas-phase nanoparticle formation method, plasma flash evaporation (PFE), can be a choice for production of nanoparticle with controlled morphology without using organic agents (**Fig. 1**). In this process, the raw powders injected are instantaneously vaporized in a thermal plasma jet and nanoparticles form via nucleation and growth of these high temperature vapors during subsequent rapid quenching [29–31]. The Ar-

H_2 reducing plasma environment and the vacuum or oxygen-less atmosphere during cooling down to the room temperature after nanoparticle formation are expected to permit slow oxidation to minimize the oxides on nanoparticles effectively. In this study, we aim to achieve low-temperature and low-pressure Cu sinter bonding in ambient air by producing slightly oxidized Cu particles using the PFE method.

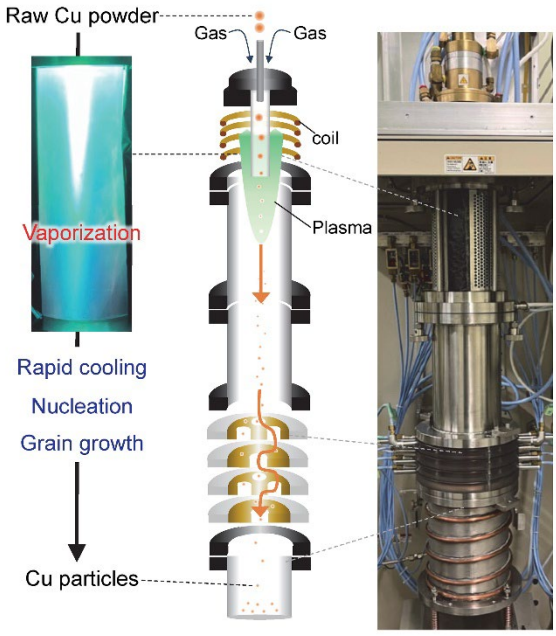

Fig. 1 Schematic and details of the Cu particle production process using the plasma flash evaporation (PFE) method.

2. Experimental procedure

2.1 Plasma flash evaporation

Commercial Cu powders (Fukuda Metal Foil & Powder Co., Ltd.) were used as raw materials of PFE process. **Fig. 2** shows a field-emission scanning electron microscopy (FE-SEM, Hitachi, S-4800) image of the Cu powders, with an average particle size of approximately 20 μm. Considering the implementations of plasma, previous studies indicated that oxygen atoms attributed to the raw material are effectively removed as the gas phase out of the reactor under an Ar-H_2 reducing plasma in the PFE process [32]. Hence, the use of plasma containing H_2 is expected to prevent internal oxidation of particles. Inductively coupled plasma (ICP) is suitable for using H_2 gas as it operates without electrodes and can be operated under oxidizing, reducing or other reactive atmospheres [33]. Based on these characteristics, a commercial Radio frequency (RF)-ICP system (JEOL, TP-40020NPS) was used for the production of Cu particles. In the RF-ICP torch, ICP is generated by coupling the electromagnetic field induced by the coil into the cylindrical discharge cavity, as shown in **Fig. 1**. A mixed Ar-H_2 plasma was used to suppress surface oxidation of the particle. The ICP is generated under the conditions listed in **Table 1**. The injected powders are expected to vaporize in the ICP torch and are rapidly quenched to form submicron particles within the water-cooled vertical chamber underneath the torch. Optical emission spectroscopy (OES) was performed to evaluate the excited Cu in the gas plasma using spectrometer (Ocean Optics, USB2000+). After plasma processing, the chamber was cooled

under vacuum for 30 min and then filled with Ar to the atmospheric pressure to prevent abrupt oxidation. This controlled cooling process is expected to minimize natural surface oxidation of the produced particles.

The morphology of the produced particles was analyzed by transmission electron microscopy (TEM, Thermo Fisher Scientific, Talos F200i) and X-ray diffraction (XRD, Bruker, D2 PHASER) measurements (CuKα radiation) in two-theta/theta method. Particle size distribution was measured through the observation using FE-SEM observations after cross-sectional milling of the particles.

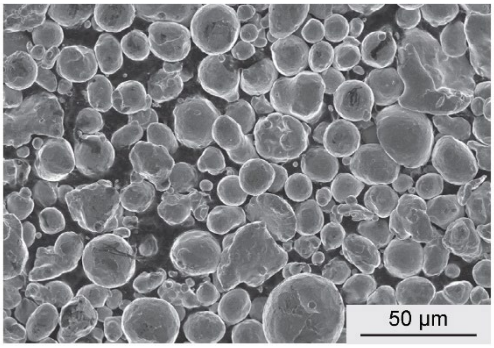

Fig. 2 FE-SEM image of Cu raw material.

Table 1 Conditions of the ICP process.

Plasma gas	RF power (kW)	Pressure (kPa)	Carrier gas: Ar (L/min)	Cooling atmosphere
$Ar+H_2$	6	30	2	Vacuum

2.2 Sinter bonding paste

The produced particles were mixed with polyethylene glycol 400 (PEG400) as a bonding paste. PEG400, a highly secure solvent, is expected to reduce surface oxides of Cu and provide oxidation resistance by remaining up to nearly 300 ℃. Terpineol was added to the paste as a thickener. For the evaluation of the reduction temperature of Cu oxidation, thermal analyses using thermogravimetry and differential thermal analysis measurements (TG-DTA, Rigaku, TG8120) were performed at a heating rate of 10 ℃/min in N_2-21%O_2 and N_2 atmospheres. In addition to raw solvents, the boding paste was analyzed by TG-DTA after preheating at 120 ℃ for 10 min for the evaporation of terpineol. To investigate the structural changes of the Cu particles during the heating process, XRD measurements and TEM observations were performed on the bonding paste at elevated temperatures. The paste was heated to 160, 180, 200, 220 ℃ at a heating rate of 1 ℃/s and held for 1 min in air and N_2 atmospheres.

2.3 Bonding experiments

Bare Cu disks (upper substrate: φ5 mm, t = 2 mm, lower substrate: φ10 mm, t = 5 mm) were used as the bonding substrates. These substrates were ultrasonically cleaned in an acetone bath for 10 min before the bonding experiment. The bonding paste was applied to the surface of the lower Cu substrate with a thickness of 50 μm, and the upper substrate was placed on the paste as shown in **Fig. 3**. After preheating at 120 ℃ for

10 min, the samples were heated to the bonding temperature of 180, 200, 220, 240 °C at a rate of 1 °C/s in an infrared heating furnace under an air atmosphere and held for 30 min at a pressure of 0.35 MPa. The joint strength was measured by a shear test with a displacement rate of 0.5 mm/s using a bond tester (Nordson DAGE, 4000Plus Bondtester). The microstructure of Cu sintered layer was observed using FE-SEM.

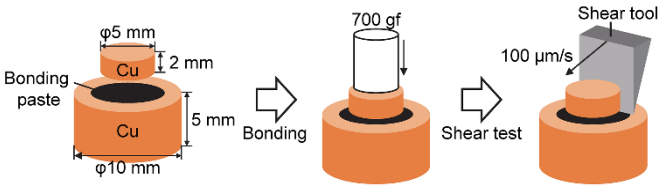

Fig. 3 Schematic diagram of Cu-Cu sinter bonding experiment.

3. Results and discussion

3.1 Analyses of Cu particles produced with PFE method

Fig. 4 shows the result of OES calibrated based on hydrogen beta rays (486.11 nm), and listed transition level of emission. NIST Atomic Spectra Database was used to evaluate the state of Cu during PFE [34]. High intensities of Cu atomic spectra were detected. It was considered that raw Cu powders were sufficiently vaporized by a thermal plasma jet, and and fine particles formed through condensation of these high temperature Cu vapors.

Fig. 5 presents the characterization results of Cu particles produced by PFE method (PFE particles) under the aforementioned conditions. The scanning TEM (STEM) images and particle size distributions reveal that the PFE particles exhibited a spherical morphology, and ranged in size from several tens of nanometers to submicron scales, significantly smaller than that of raw powders (**Fig. 5**(a), (b)). This suggests that the particles were formed from vaporized raw powders. It is also presumed that any organic matter covering the raw materials was eliminated during the process. **Fig. 5**(c) shows the nanobeam electron diffraction (NBD) patterns obtained from the surface of a Cu particle. These patterns indicated the presence of slight CuO localized on the surface of the particles with an approximately thickness of 2 nm. Similarly, XRD results (**Fig. 5**(d)) confirm the presence of CuO in the PFE particles, with no detectable Cu_2O. This absence of Cu_2O in the PFE particles contrasts with previous studies, which reported its reduction to Cu nanoparticles during the bonding process [19].

The formation of only a slight amount of CuO, with the absence of Cu_2O, on the surface of PFE particles is likely attributed to oxidation suppression achieved by using Ar-H_2 mixed-gas plasma and minimal oxidation during the cooling process. Furthermore, the slight presence of CuO might contribute to suppressing the excessive aggregation of the produced particles.

In the incipient surface oxidation process of Cu(111), it has been reported that Cu atoms at the gas-solid interface react rapidly with O_2 with only a small thermodynamic resistance, thereby forming CuO nano-islands [35]. As the oxidation progresses, these CuO nano-islands grow, and a Cu_2O layer forms between the surface CuO layer and interior Cu layer. When this finding can be applied to the present study, it is inferred that the PFE particles exhibit a lower oxidation compared to the particles with a covered Cu_2O layer. Consequently, PFE method was found to successfully fabricate slightly oxidized Cu nano- to submicron-sized particles.

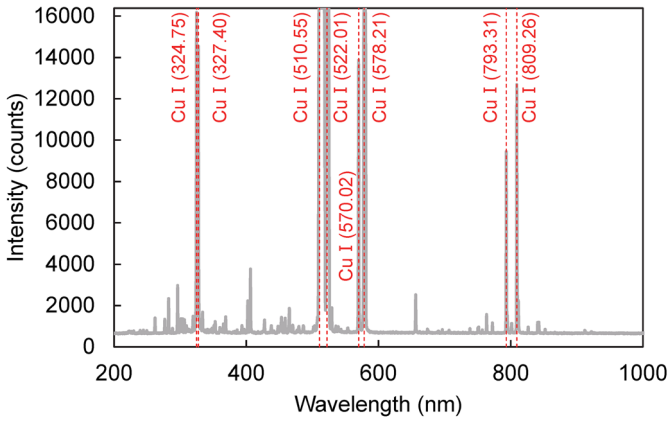

Fig. 4 Result of OES during PFE method. The dot lines show the references Cu atomic spectra.

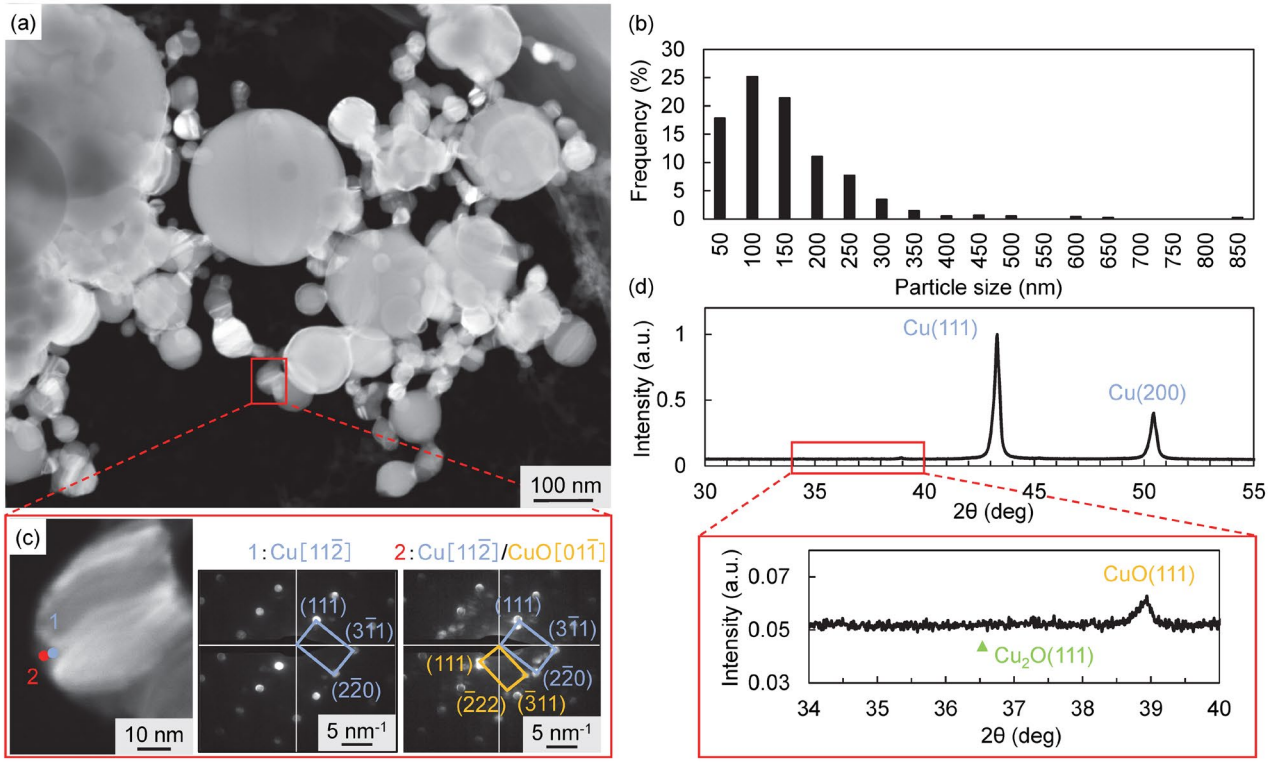

Fig. 5 Characterization of Cu particles produced by PFE method. (a) Dark-field STEM image of Cu particles. (b) Particle distribution.(c) Nanobeam electron diffraction patterns obtained from a Cu particle surface. (d) XRD pattern.

3.2 Analyses of Cu bonding paste mixed with PEG400

Fig. 6 shows the TG-DTA results for PEG400 and terpineol in N_2-21%O_2, and Cu bonding paste in N_2-21%O_2 and N_2 atmospheres. Terpineol evaporated above 120 °C (**Fig. 6**(a)), while PEG400 evaporated above 200 °C, and combusted above 250 °C (**Fig. 6**(b)). The bonding paste exhibited a slight weight loss at approximately 120 °C without any exothermic reaction and a gradual decrease in weight above 200 °C under both atmospheres (**Fig. 6**(c), (d)). Furthermore, a marked change in weight loss behavior accompanied by an exothermic reaction occurred at 220 °C. In N_2-21%O_2, a large exothermic reaction was also confirmed above 250 °C (**Fig. 6**(c)). The weight loss at 120 °C and the gradual decrease in weight above 200 °C are attributed to the evaporation

of terpineol and PEG400, respectively. The large reaction above 250 °C in N_2-21%O_2 corresponds to a combustion reaction of PEG400. In N_2, no exothermic reaction of the paste was observed above 250 °C due to the absence of oxygen in atmosphere (**Fig. 6**(d)). However, since no exothermic reaction was observed at approximately 220 °C in the solvents, it is inferred that the reaction at 220 °C is caused by the redox reaction between Cu particles and PEG400.

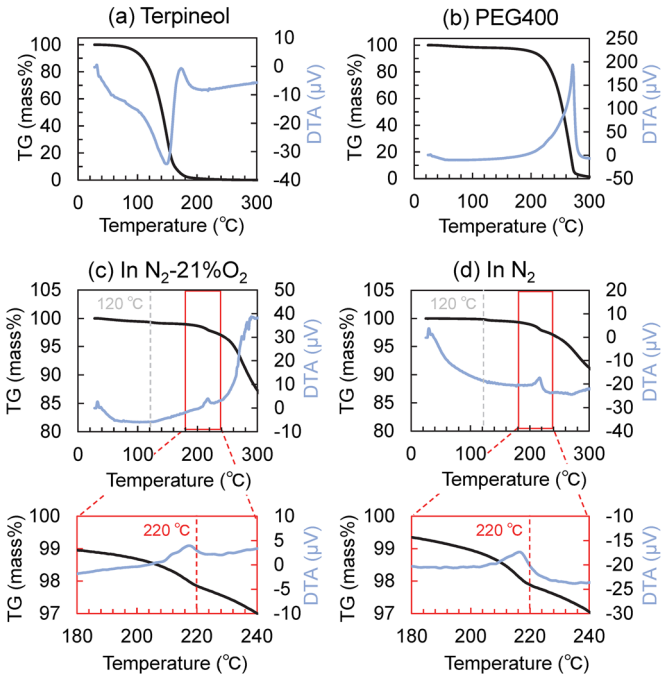

Fig. 6 TG-DTA traces at a heating rate of 10 °C/min: (a) terpineol and (b) PEG400 in N_2-21%O_2, and Cu bonding paste (c) in N_2-21%O_2 and (d) in N_2.

XRD analyses and TEM observations of the heated paste were conducted to investigate microstructural change of the particle surface caused by the reaction at around 220 °C. **Fig. 7** shows XRD results of the paste heated to the elevated temperature up to 220 °C. The intensity values were normalized by dividing by the intensity of the Cu(111) peak. A broad Cu_2O(111) peak started to appear above 160 °C under both atmospheric conditions, and the intensity of Cu_2O peak gradually increased with rising temperature. Further, intensity of the Cu_2O peak in the paste heated in air was larger than that heated in N_2. The broad Cu_2O peak indicated that morphology of Cu_2O is amorphous or nanoparticles. However, the intensity of CuO peak, which was surface oxide of PFE particles, remained constant regardless of the heating temperature.

Fig. 8 shows the results of TEM observation of the paste after preheating and subsequent heating to 180 °C and 220 °C in air. Bright-field TEM images and selected area electron diffraction patterns obtained from the surface of Cu particles heated to 180 °C revealed the presence of Cu_2O nanoparticles in the remaining solvent (**Fig. 8**(a), (c)). At a temperature of 220 °C, both Cu_2O and Cu nanoparticles were observed in the remaining solvent, indicating the progression of bridging between Cu particles.

Considering the cause of Cu_2O generation above 160 °C, CuO which can be reduced to Cu_2O seemed to be unrelated to Cu_2O generation since the intensity of CuO was constant regardless of the temperature as

mentioned in **Fig. 7**. The generation of Cu_2O during heating in N_2 atmosphere, where oxygen is minimal, suggests that Cu_2O does not stem from the oxidation of Cu particles. Previous studies have reported that PEG400 is utilized as a solvent, complexed agent, and reducing agent in the wet chemical synthesis of Cu_2O, where it plays a key role in producing polycrystalline Cu_2O [36,37]. Based on the prior knowledge, it is hypothesized that Cu_2O nanoparticles are produced through the precipitation from a Cu complex derived from the reaction with PEG400, particularly at unoxidized areas or grain boundaries of surface oxide. It is also postulated that the higher intensity of Cu_2O in air could be due to the promoted reactions with PEG400, compared to in N_2. The generation of Cu nanoparticles at around 220 °C is likely attributed to the reduction of Cu_2O nanoparticles, as XRD analysis demonstrated that the reduction of Cu_2O was complete at 220 °C after a holding time of 30 min in N_2 atmosphere as shown in **Fig. 7**(b). Accordingly, the generation of Cu_2O nanoparticles is expected to lower the reduction temperature of Cu oxide, thus lowering Cu sinter bonding temperature.

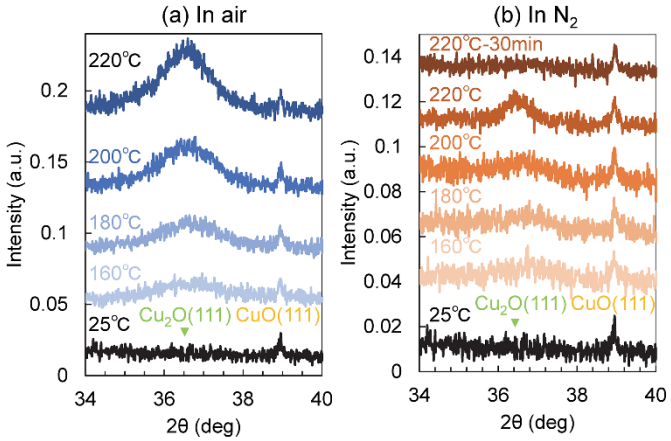

Fig. 7 XRD patterns of synthesized Cu bonding paste heating at 25, 160, 180, 200, and 220 °C.

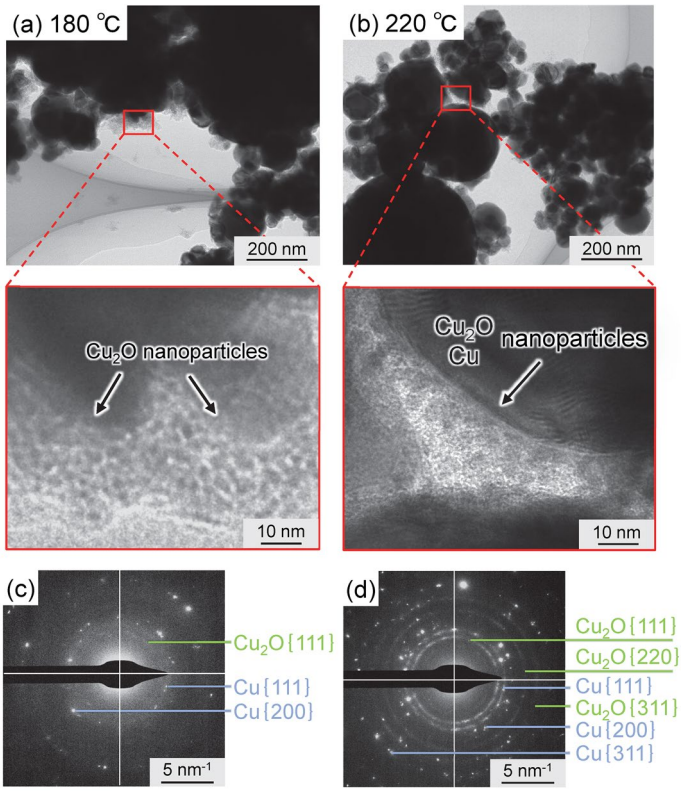

Fig. 8 TEM observation results of the Cu bonding paste. (a), (b) Bright-field TEM images and (c), (d) selected area electron diffraction patterns of the pastes heated to 180, 220 °C, respectively.

3.3 Cu-Cu sinter bonding results

Fig. 9 shows the shear strength of Cu sinter joints bonded in air and the density of the sintered layer, estimated from cross-sectional analysis. **Figs. 10** and **11** exhibit cross-section of Cu sintered joints and fractured surfaces after shear testing. At a sintering temperature of 180 °C, Cu particles in the sintered layer showed no change in morphology, remaining as nano- to submicron-sized spherical particles, whereas Cu_2O nanoparticles formed above 160 °C in the paste. It is inferred that the PEG400 does not combust to reduce Cu_2O at the sintering temperature as the weight loss of PEG400 is not confirmed below 200 °C (**Fig. 6**(b)). At sintering temperatures of 200 °C or higher, necking of Cu particles occurred, leading to increases in both the shear strength and the density of the sintered layer. At 220 °C, the shear strength reached approximately 20 MPa. As confirmed in **Fig. 7**, the reduction of Cu_2O nanoparticles to Cu nanoparticles is completed at 220 °C, suggesting that the sinterability increases significantly from 200 to 220 °C due to the bridging of Cu nanoparticles. Neck formation of the particles (**Figs. 10**, **11**) revealed the presence of Cu on their outermost surface, although residual CuO, the surface oxide of PFE particles, remained as confirmed by XRD analyses (**Fig. 7**). This suggests that initial surface CuO is scattered and sintering proceeded with scattered surface CuO. At 240 °C, stereo micrographs of the fracture surface showed oxidation at the edges, likely caused by the combustion of PEG400. However, the sintering among PFE particles proceeded more rapidly compared to the layer bonded at 220 °C. Assuming that only the Cu_2O reduction process occurs at 220 °C or higher, the amount of generated Cu_2O and Cu nanoparticles would reach equilibrium at a certain temperature, limiting further sintering progress. Therefore, the progress of sintering from 220 °C to 240 °C implies that the complexation of Cu with PEG400 and the precipitation of Cu_2O nanoparticles continued during the Cu_2O reduction process.

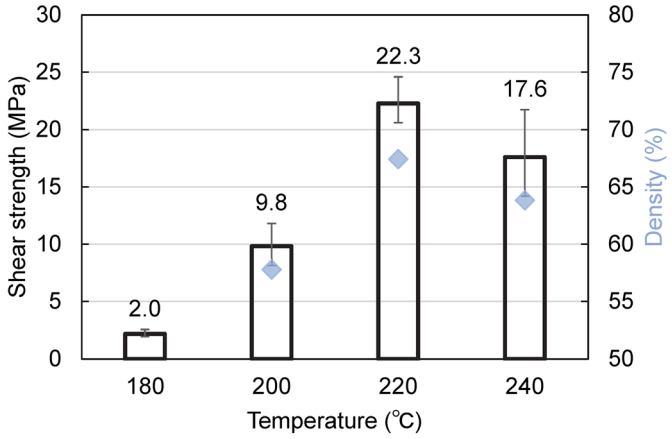

Fig. 9 Shear strength of Cu-Cu joints bonded at 180–240 °C for the holding time of 30 min under 0.35 MPa in air.

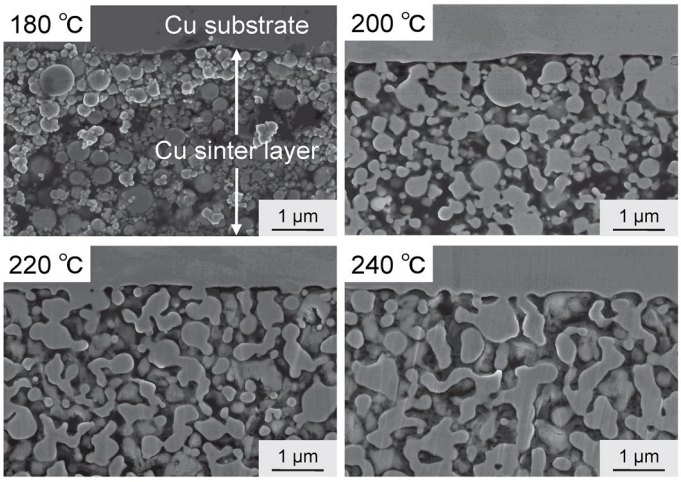

Fig. 10 Cross-sectional FE-SEM image of Cu-Cu joints bonded at 180–240 °C.

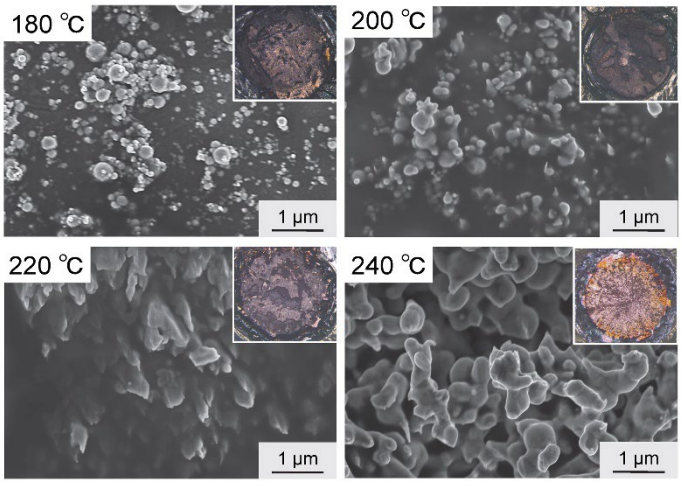

Fig. 11 Stereo micrographs and FE-SEM images of fracture surface of the Cu-Cu joints bonded at 180–240 °C.

TEM observations were conducted to investigate the surface structure of the sintered Cu bonded at 220 °C as shown in **Fig. 12**. A typical electron diffraction pattern obtained from the sintered layer exhibited the presence of polycrystalline Cu_2O in addition to Cu (**Fig .12**(b)). The detailed observation revealed that slight Cu_2O nanoparticles (**Fig. 12**(c)) and residual PEG400 (**Fig. 12**(d)) were present on the sintered surface. The small quantity of Cu_2O nanoparticles suggests that the reduction of Cu_2O to Cu nanoparticles occurred preferentially at 220°C, facilitating sufficient neck formation through the sintering of Cu nanoparticles. Additionally, the presence of residual PEG400 would provide the layer with oxidation resistance in air.

Consequently, Cu-Cu sinter bonding was successfully achieved at 220 °C due to the complete reduction of Cu_2O nanoparticle and the high sinterability of the Cu nanoparticles formed.

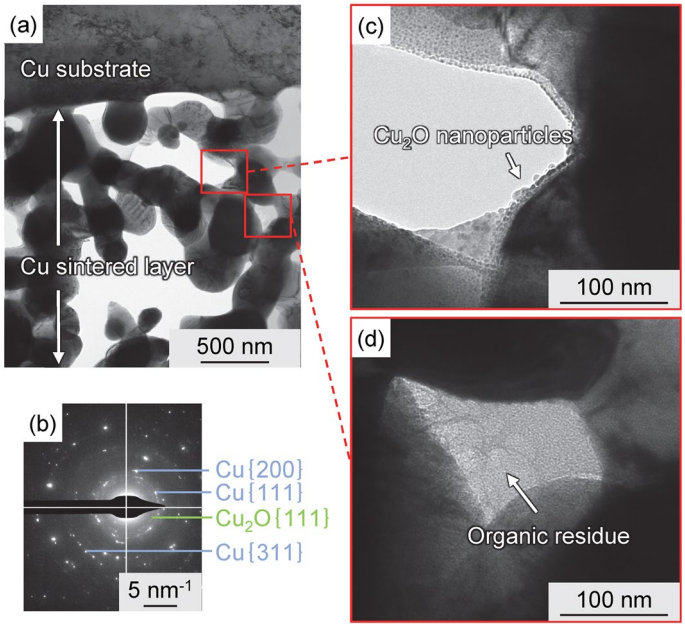

Fig. 12 TEM observation result of Cu sintered layer bonded at 220 °C. (a) Bright-filed TEM image of the appearance of sintered layer and (b) typical diffraction pattern. (c), (d) Magnified views of the layer.

3.4 Sintering process using Cu particles produce by PFE method

Fig. 13 illustrates the sintering process of PFE particles. PFE particles contain scattered CuO in surface area of approximately 2 nm. In the Cu bonding paste mixed with PEG400, Cu complexes with PEG400 through unoxidized areas and grain boundaries within the surface oxide. When the temperature of the paste increased to 160 °C or higher, Cu_2O nanoparticles precipitate due to the reaction of hydroxyl groups in PEG400 with dissolved Cu. At 220 °C, Cu_2O nanoparticles are reduced to Cu nanoparticles due to the evaporation of PEG400 as a reducing solvent. It is assumed that the reduction of Cu_2O occurs preferentially while the complexation of Cu with PEG400 and the precipitation of Cu_2O nanoparticles continued. The generated Cu nanoparticles form a sintered Cu structure through necking with unoxidized areas of Cu particles. In this process, the reduction temperature for Cu formation from Cu_2O is lowered due to the morphology of the Cu_2O nanoparticles and the high sinterability of the Cu nanoparticles, contributing to a lower bonding temperature.

As a result, it was revealed that minimizing the surface oxide of particles enables the formation of Cu_2O nanoparticles at elevated temperatures, which facilitates their complete reduction to Cu nanoparticles at a lower temperature. In this study, we adopted a gas phase method to prioritize producing particles without covering

agent to eliminate factors that inhibit sintering. Furthermore, the PFE method demonstrated the ability to produce fine particles while effectively controlling the atmosphere during the gas-phase process. The PFE method successfully minimized surface oxides in this study, enabling low-temperature and low-pressure bonding in air through the in-situ formation and reduction of Cu_2O nanoparticles, driven by the reaction between the PFE-derived particles and PEG400. While the PFE method demonstrated successful bonding results in this study, similar particles could likely be produced by other methods, leading to comparable bonding results.

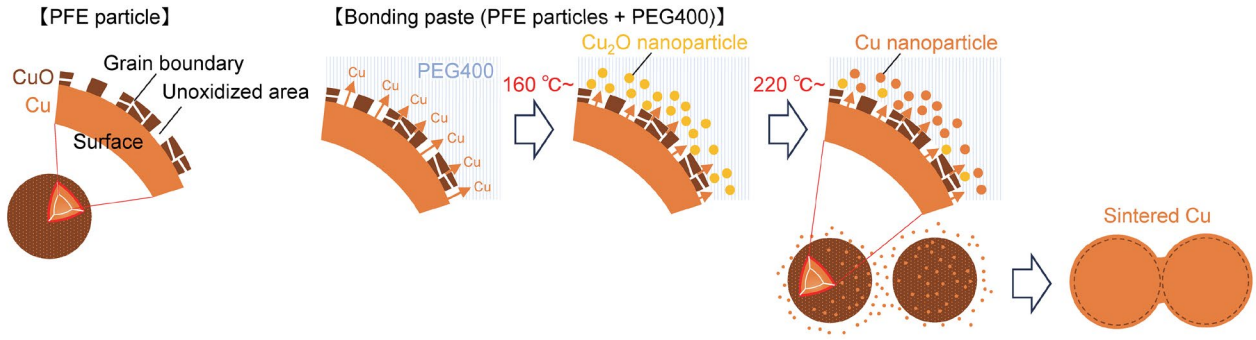

Fig. 13 Schematic diagram of sintering process of PFE particles.

4. Conclusions

In this study, we successfully developed a low-temperature and low-pressure Cu-Cu sinter bonding process in ambient air by utilizing nano- to submicron-sized Cu particles produced via the plasma flash evaporation (PFE) method and polyethylene glycol 400 (PEG400) as a reducing agent. The primary findings of this work are summarized as follows:

- Submicron-sized Cu particles with a surface CuO of approximately 2 nm were produced using the PFE method. Oxidation was effectively suppressed by the Ar-H_2 plasma during particle production, with slight oxidation occurring during the cooling step under vacuum.
- During heating of the Cu bonding paste, Cu_2O nanoparticles were formed above 160 °C through precipitation from a Cu complex derived from the reaction with PEG400. These Cu_2O nanoparticles were subsequently reduced to Cu nanoparticles at 220 °C due to the partial combustion of PEG400, which acted as a reducing agent.
- Cu-Cu sinter bonding was achieved at 220 °C under 0.35 MPa in ambient air. The in-situ generated Cu nanoparticles acted as bridges between submicron Cu particles, facilitating sintering and forming a dense, oxidation-resistant bonding layer.
- The in-situ reactions of Cu particles and PEG400, involving temporary oxide formation and reduction, demonstrated the potential to achieve low-temperature and low-pressure bonding in ambient air for particles produced by other methods as well.

Declarations

Conflict of interest

The authors declare that they have no known competing financial interests or personal relationships that could have appeared to influence the work reported in this paper.

Author contributions

All authors contributed to the study conception and design. Material preparation, data collection and analysis were performed by M. Oba, T. Matsuda, M. Dougakiuchi, and S. Okubo. The first draft of the manuscript was written by M. Oba and edited by T. Matsuda and M. Kambara. All authors read and approved the final manuscript.

Funding

This work was supported in part by the Japan Society for the Promotion of Science (JSPS) KAKENHI (Grant Numbers 22H01832 and 23K23100) and Iketani Science and Technology Foundation (Grant Number 0361033-A).

Data Availability

The datasets generated and analyzed during the current study are available from the corresponding author upon reasonable request.

References

1. E. Ugur, F. Yang, S. Pu, S. Zhao, and B. Akin, IEEE Trans. Ind. Appl. **55**, 2858 (2019) https://doi.org/10.1109/TIA.2019.2891214

2. L. C. Yu, G. T. Dunne, K. S. Matocha, K. P. Cheung, J. S. Suehle, and K. Sheng, IEEE Trans. Device Mater. Reliab. **10**, 418 (2010) https://doi.org/10.1109/TDMR.2010.2077295

3. J. Millan, P. Godignon, X. Perpina, A. Perez-Tomas, and J. Rebollo, IEEE Trans. Power Electron. **29**, 2155 (2014) https://doi.org/10.1109/TPEL.2013.2268900

4. K. Hamada, M. Nagao, M. Ajioka, and F. Kawai, IEEE Trans. Electron Devices **62**, 278 (2015) https://doi.org/10.1109/TED.2014.2359240

5. T. Iwashige, T. Endo, K. Sugiura, K. Tsuruta, Y. Sakuma, Y. Oda, C. Chen, S. Nagao, T. Sugahara, and K. Suganuma, J. Mater. Sci. **55**, 644 (2020) https://doi.org/10.1007/s10853-019-04028-z

6. J. Keller, D. Baither, U. Wilke, G. Schmitz, Acta Mater. **59**, 2731 (2011) https://doi.org/10.1016/j.actamat.2011.01.012

7. A. Elmahfoudi, S. Fürtauer, A. Sabbar, and H. Flandorfer, Thermochim. Acta **534**, 33 (2012) https://doi.org/10.1016/j.tca.2012.01.024

8. E. Ide, S. Angata, A. Hirose, K. F. Kobayashi, Acta Mater. **53**, 2385 (2005) https://doi.org/10.1016/j.actamat.2005.01.047

9. C. Chen, K. Suganuma, Mater. Des. **162**, 311 (2019) https://doi.org/10.1016/j.matdes.2018.11.062

10. D. Ishikawa, B. N. An, M. Mail, H. Wurst, B. Leyrer, T. Blank, M. Weber, and H. Nakako, Trans. Jpn. Inst. Electron. Packag. **13**, E20-003-1 (2020) https://doi.org/10.5104/jiepeng.13.e20-003-1

11. E. B. Choi, Y. J. Lee, J. H. Lee, J. Alloy. Compd. **897**, 163223 (2022) https://doi.org/10.1016/j.jallcom.2021.163223

12. Y. Gao, Y. bo Xiao, Z. Q. Liu, Y. Liu, and R. Sun, J. Mater. Sci. Mater. Electron. **33**, 3576 (2022) https://doi.org/10.1007/s10854-021-07551-5
13. M. Nishimoto, R. Tokura, M. T. Nguyen, and T. Yonezawa, Mater. Trans. **63**, 663 (2022) https://doi.org/10.2320/matertrans.MT-N2021004
14. Y. Yuan, M. Zhang, J. Li, and Z. Q. Liu, J. Mater. Sci. Mater. Electron. **34**, 1675 (2023) https://doi.org/10.1007/s10854-023-11095-1
15. W. L. Choi, Y. S. Kim, K. S. Lee, and J. H. Lee, J. Mater. Sci. Mater. Electron. **30**, 9806 (2019) https://doi.org/10.1007/s10854-019-01317-w
16. T. Matsuda, S. Yamada, S. Okubo, and A. Hirose, J. Mater. Sci. **58**, 15617 (2023) https://doi.org/10.1007/s10853-023-08976-5
17. J. Yan, G. Zou, A. Hu, and Y. N. Zhou, J. Mater. Chem, **21**, 15981 (2011) https://doi.org/10.1039/C1JM12108A
18. J. Liu, Y. Mou, J. Liu, Y. Peng, and M. Chen, IEEE Trans. Compon. Packaging mauf. Technol. **12**, 878 (2022) https://doi.org/10.1109/TCPMT.2022.3163175
19. D. Yamagiwa, T. Matsuda, H. Furusawa, K. Sato, H. Tatsumi, T. Sano, Y. Kashiba, and A. Hirose, J. Mater. Sci. Mater. Electron. **32**, 19031 (2021) https://doi.org/10.1007/s10854-021-06418-z
20. J. Li, Q. Liang, T. Shi, J. Fan, B. Gong, C. Feng, J. Fan, G. Liao, and Z. Tang, J. Alloys. Compd. **772**, 793 (2019) https://doi.org/10.1016/j.jallcom.2018.09.115
21. Y. Gao, W. Li, C. Chen, H. Zhang, J. Jiu, C. F. Li, S. Nagao, and K. Suganuma, Mater. Des. **160**, 1265 (2018) https://doi.org/10.1016/j.matdes.2018.11.003
22. S. Liu, L. Yang, J. Xin, X. Lv, Y. Chen and Y. Liu, J. Mater. Sci. Mater. Electron. **35**, 1493 (2024) https://doi.org/10.1007/s10854-024-13220-0
23. X. Liu and H. Nishikawa, J. Mater. Sci. Mater. Electron. **28**, 5554 (2017) https://doi.org/10.1007/s10854-016-6220-8
24. E. B. Choi and J. H. Lee, Appl. Surf. Sci. 546, 149156 (2021) https://doi.org/10.1016/j.apsusc.2021.149156
25. T. Yonezawa, Y. Uchida, and Y. Abe, J. Nanosci. Nanotechnol. **14**, 5402 (2014) https://doi.org/10.1166/jnn.2014.7919
26. M. S. Aguilar, R. Esparza, G. Rosas, Trans. Nonferr. Met. Soc. China. **29**, 1510 (2019) https://doi.org/10.1016/S1003-6326(19)65058-2
27. P. G. Jamkhande, N. W. Ghule, A. H. Bamer, and M. G. Kalaskar, J. Drug Deliv. Sci. Tech. **53**, 101174 (2019) https://doi.org/10.1016/j.jddst.2019.101174
28. A. Khan, A. Rashid, R.Younas, Ren.Chong, Int. Nano Lett. **6**, 21 (2016) https://doi.org/10.1007/s40089-015-0163-6
29. G. Mauer and R. Vaßen, Surf. Coat. Technol. **371**, 417 (2019) https://doi.org/10.1016/j.surfcoat.2018.06.086
30. R. Ohta, K. Fukada, T. Tashiro, M. Dougakiuchi, and M. Kambara, J. Phys. D **51**, 105501 (2018) https://doi.org/10.1088/1361-6463/aaab37
31. M. Kambara, M. Fukuda, R. Ohta, T. Tanaka, A. Takeuchi, M. Dougakiuchi, and K. Fukuda, Jpn. J. Appl. Phys. **60**, 105507 (2021) https://doi.org/10.35848/1347-4065/ac28e1

32. R. Ohta, T. Tanaka, A. Takeuchi, M. Dougakiuchi, K. Fukuda, and M. Kambara, J. Phys. D **54**, 494002 (2021) https://doi.org/10.1088/1361-6463/ac23ff
33. J. Nava-Avendaño, J. Veilleux, J. Phys. D **50**, 163001 (2017) https://doi.org/10.1088/1361-6463/aa6245
34. Kramida, A., Ralchenko, Yu., Reader, J., and NIST ASD Team (2024). NIST Atomic Spectra Database (ver. 5.12) https://physics.nist.gov/asd
35. C. Zheng, J. Cao, Y. Zhang, and H. Zhao, Energy Fuels **34**, 8718 (2020) https://doi.org/10.1021/acs.energyfuels.0c00941
36. Y. Xu, X. Jiao, and D. Chen, J. Phys. Chem. C **112**, 16769 (2008) https://doi.org/10.1021/jp8058933
37. S. J. Chen, X. T. Chen, Z. Xue, L. H. Li, and X. Z. You, J. Cryst. Growth **246**, 169 (2002) https://doi.org/10.1016/S0022-0248(02)01902-4